RSC Advances

PAPER

View Article Online
View Journal | View Issue

Cite this: *RSC Adv.*, 2021, **11**, 7808

The effects of Fe-doping on MnO_2: phase transitions, defect structures and its influence on electrical properties

E. Hastuti, [ab] A. Subhan, [c] P. Amonpattaratkit,[d] M. Zainuri[a] and S. Suasmoro *[a]

Received 9th December 2020
Accepted 28th January 2021

DOI: 10.1039/d0ra10376d

rsc.li/rsc-advances

The composition of $Mn_{1-x}Fe_xO_2$ ($x = 0$–0.15) was synthesized by a hydrothermal method at 140 °C for 5 hours of reaction time. Investigations were carried out including XRD, FTIR, Raman spectroscopy, FESEM, and TEM for crystallographic phase analysis. Furthermore, XPS and XAS were used to analyze the oxidation states of Mn and dopant Fe in the octahedron sites. For electrical characterizations, an impedance analyzer was used to explore the conductivity and dielectric properties. It was discovered that the undoped MnO_2 possessed an α-MnO_2 structure performing (2×2) tunnel permitting K^+ insertion and had a nanorod morphology. The Fe ion that was doped into MnO_2 caused a phase transformation from α-MnO_2 to Ramsdellite R-MnO_2 after $x = 0.15$ was reached and the tunnel dimension changed to (2×1). Furthermore, this caused increased micro-strain and oxygen vacancies. An oxidation state analysis of Mn and substituted Fe in the octahedron sites found mixed 3+ and 4+ states. Electrical characterization revealed that the conductivity of Fe-doped MnO_2 is potentially electron influenced by the oxidation state of the cations in the octahedron sites, the micro-strain, the dislocation density, and the movement of K^+ ions in the tunnel.

1. Introduction

In recent years, manganese dioxide (MnO_2) materials have attracted the attention of researchers due to its application in electrochemical energy storage electrodes, and also due to its novel chemical and physical properties as a result of its excellent structural flexibility.[1] MnO_2-Based electrodes store electric charge using a pseudocapacitive mechanism.[2] The theoretical capacitance of manganese oxide can be up to 1300 F g^{-1},[3] but the electrochemical reversibility of the redox transition of manganese dioxide is usually low in applications, and pure manganese dioxide has a poor capacitive response.[3] Despite this, manganese oxide is seen as a potentially useful material for pseudocapacitors because of its low cost, abundance in the earth, and environmental friendliness.[4]

With respect to the structure, manganese dioxide exhibits polymorphism with some crystal structures based on various linkages of basic [MnO_6] octahedral units, comprising α-MnO_2, β-MnO_2, γ-MnO_2, δ-MnO_2, λ-MnO_2, ε-MnO_2, and R-MnO_2, respectively.[5] The different structures can be described by the size of the tunnel, which is determined by the number of octahedral subunits ($n \times m$), where n and m stand for the dimensions of the tunnels in the two directions perpendicular to the chains of the edge-sharing octahedral MnO_6.[6] Among these, the nanostructure α-MnO_2 shows the highest charge storage capacity, due to the occurrence of an edge-sharing MnO_6 octahedral, leading to the formation of 1D (2×2) and (1×1) tunnels extended in a direction parallel to the *c*-axis of the tetragonal unit cell *via* linking at the corners.[7,8] The (2×2) tunnels are stabilized by cations (K^+, Li^+, and Na^+) and the (1×1) tunnels are unfilled.[9]

In order to enhance the properties, up until now, various synthesis methods have been developed, namely sol–gel,[10] co-precipitation,[11] electrodeposition,[12] and hydrothermal reaction.[13] These various methods are able to reduce the crystal size, enlarge the surface area for the enhancement of the ion diffusion rate[8] and finally improve the supercapacitive performance of MnO_2. Out of these methods of preparation, it appears that the hydrothermal method is the simplest and most inexpensive. Hydrothermal synthesis is challenging for producing diverse polymorphism in metal oxide crystalline systems that proceed at a low temperature.[14] Furthermore, the Mn oxidation state was reported as an additional important factor in determining and optimizing the electrochemical properties. The charge storage mechanism arises from alternating between the Mn^{3+} and Mn^{4+} oxidation states at or near the surface of the MnO_2 nanostructures, and this can lead to a slight distortion in the octahedral MnO_6 structure, due to a Jahn–Teller effect.[15] The

[a]*Institute of Technology 'Sepuluh Nopember' Surabaya, Kampus ITS Sukolilo, Surabaya 60111, Indonesia. E-mail: suasm@its.ac.id; Fax: +62315943351; Tel: +6282245157676*

[b]*Universitas Islam Negeri 'Maulana Malik Ibrahim' Malang, Indonesia*

[c]*Research Center for Physics, Indonesian Institute for Science (LIPI), Serpong, Indonesia*

[d]*Synchroton Light Research Institute (Public Organisation), 111 University Avenue, Muang, Nakhon Ratchasima 30000, Thailand*

electrochemical properties can be improved by doping with metal ions, such as V, Ru, Ag, Co, Ni, Sn, Cu^{2+}, Co^{2+}, Ni^{2+},[16–21] and Fe.[17,22,23] Among these ions, Fe can substitute for Mn or occupy the tunnels of MnO_2 (ref. [24]) and is highly beneficial for balancing the stabilization of the tunnel structures with a suitable amount of Fe-doped into MnO_2. Wang[25] reported that Fe-doped MnO_2 nanostructures of different phases depend on the percentage of Fe (α-MnO_2/R-MnO_2/ε-MnO_2) and that they obtained good rate capability of capacitance retention and high energy density. Fe can be considered as a transition metal that possesses multivalences of 2+, 3+ and, recently reported, 4+ in an octahedron environment.[26] When the metal substitutes Mn in the octahedron site, it then create defects Fe''_{Mn}, Fe'_{Mn} and Fe^{x}_{Mn}, and $V^{\bullet\bullet}_{O}$ for neutralization, and these will affect the electrical properties. Moreover, it decreases the average crystallite size, indicates the appearance of lattice strain, and disrupts chemical bonding, yielding a modification to the 3d configuration of either $3d^4$ Mn^{3+} or $3d^5$ Mn^{2+}.

Considering the above-mentioned possible defects, it is intriguing to carry out further exploration of its presence in the sample. In this study, the lattice strain, oxidation state, and local structure were investigated. The study will focus on the structural evolution and defect structures as a result of the dopant quantity, and then the influence on the electrical properties. For this purpose, an MnO_2 electrode material will be synthesized through a hydrothermal method with various concentrations of Fe_2O_3 dopant.

2. Experimental

2.1. Materials preparation

Undoped and Fe-doped (0.05–0.15 mole%) MnO_2 samples were prepared by a hydrothermal method.

For the synthesis of undoped MnO_2, 3.32 mmol potassium permanganate ($KMnO_4$) was dissolved in water (60 mL) at room temperature, and then concentrated HCl was added (37%, 2 mL). The mixture was stirred vigorously for several minutes and then transferred into a Teflon-lined stainless-steel autoclave (capacity of 100 mL). The autoclave was sealed and was maintained at 140 °C for 5 hours, before being cooled down to room temperature. To synthesize the Fe-doped samples, $FeCl_3 \cdot 6H_2O$ was used as a dopant reagent in the above solution and the method was carried out in a similar way. The precipitates were isolated by filtration and were washed with water and ethanol several times to remove possible impurities. The sample was then dried in an oven at 80 °C for 3 hours.

2.2. Characterization

The phases and crystalline structures of the samples were analyzed through X-ray diffraction (XRD), utilizing Cu Kα radiation operating at 30 mA and 40 kV. The phases were identified by employing Match! Software, while the structures of the samples were deduced using Rietveld's refinement with the Rietica software. Further analysis was carried out using Fourier Transform Infrared spectroscopy (FTIR) and Raman spectroscopy with a 785 nm wavelength laser.

The X-ray absorption near edge structure (XANES) and extended X-ray absorption fine structure (EXAFS) of the Mn–K edge and Fe–K edge were recorded at the BL-8 beamline of the Synchrotron Light Research Institute (SLRI). All spectra were collected at room temperature in transmission mode. The monochromator energy was calibrated with Mn and Fe foil. The obtained data were processed using ATHENA and ARTEMIS software. X-ray photoelectron spectroscopy (XPS) data were obtained with an Axis Ultra DLD system equipped with an Al monochromatic.

The microstructures and morphologies of the as-prepared samples were characterized by scanning electron microscopy (FESEM/SEM), attached to an energy-dispersive X-ray analysis (EDAX) analyzer, in order to measure the sample compositions. The crystal structure details were further characterized by transmission electron microscopy (TEM) and high-resolution transmission electron microscopy (HRTEM). Selected area electron diffraction (SAED) patterns were recorded and analyzed using Crystbox software to obtain *d*-spacing.[27]

The electrical analysis was performed on a powder uniaxially pressed at $\approx$0.4 MPa with a diameter of 13 mm. The pellets were sandwiched between two copper electrodes under spring-loaded pressure to ensure an ohmic contact. The setup was measured with an (ac) Solartron impedance analyzer in the frequency range of 0.1 Hz–32 MHz and at a voltage of 1 V.

3. Results and discussion

3.1. Synthesis of α-MnO_2

Fig. 1 shows the XRD patterns of the synthesized powder at different temperatures and soaking times during the hydrothermal processes. At 100 °C for 1 hour, the pattern displays a δ-MnO_2 structure. However, the amorphous phase is notable. Furthermore, the increased temperature of the reaction to 140 °C to the peaks in the δ-MnO_2 phase is remarkable, although the yield only reaches 60%. With an increase in the reaction time of the hydrothermal reaction to 3 hours, the phase transformed from δ-MnO_2 to α-MnO_2 and, correspondingly, the yield increased to 97%. Furthermore, with a longer reaction time of up to 7 hours, the yield succeeds at being asymptotic up to 100% (Fig. 1b), while the α-MnO_2 phase is preserved.

With the prolongation of the reaction time at 140 °C, there is structural transformation and growth. With the extension of the reaction time, the crystallinity gradually increases, and a phase transformation from δ to α-MnO_2 must have taken place in the formation of α-MnO_2. Studies on structural growth[28] initially show that δ-MnO_2 has a layered structure form that tends to curl with the driving force of increased temperature and pressure, continuing to develop and then transform to the α-MnO_2 phase, as indicated in Fig. 1a.

3.2. Microstructure and structural analysis

After considering the previous study, the following synthesis was carried out at 140 °C for 5 hours of soaking time. Fig. 2 shows the XRD patterns of the Fe-doped MnO_2 samples, $Mn_{1-x}Fe_xO_{2-\delta}$ ($x = 0$–0.15). The patterns are similar for $x = 0$ up

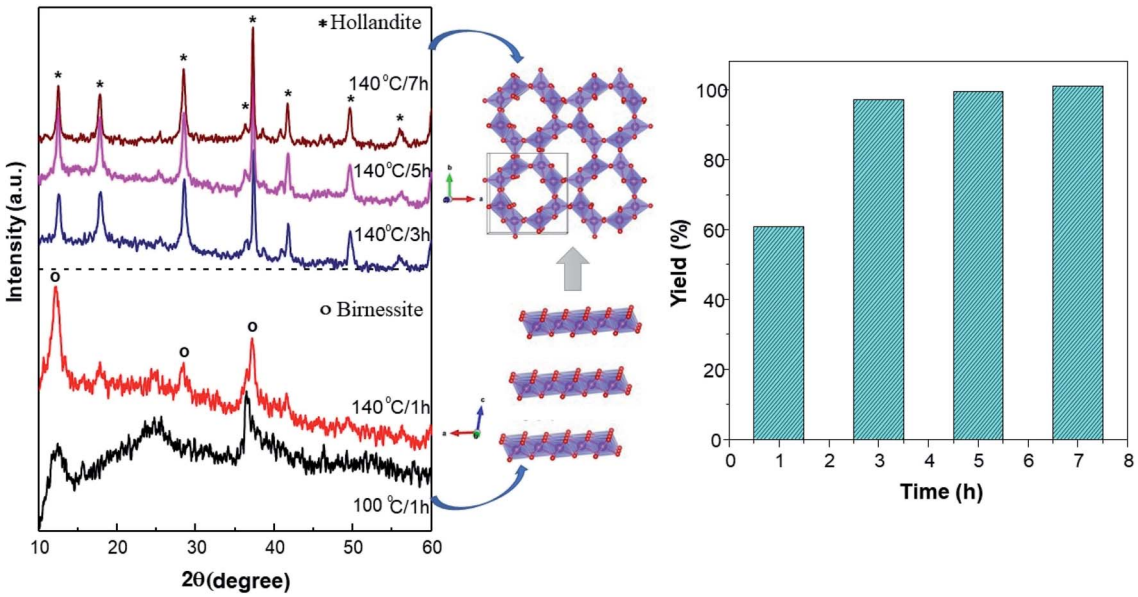

Fig. 1 Synthesis of MnO_2 through a hydrothermal method. (a) The XRD patterns of MnO_2 and possible crystal growth during synthesis at different temperatures and reaction time. (b) Reaction yields.

to $x = 0.10$ and can be assigned as α-MnO_2 using the Match 2 software. This presents a hollandite-type structure (tetragonal, space group $I4/m$) that was similarly reported by Kondrashef (1951). No additional peaks that can be assigned to the compounds of the doped materials appear in the samples, indicating that the doped materials are well incorporated into the structure and, considering the ionic radius of Fe^{3+} (73 pm) and assuming that the high spin and low spin forms of Fe^{3+} co-exist, its radius is quite similar to that of Mn^{4+} (67 pm).

When x was increased to 0.15, two important peaks were observed at $2\theta \approx 22°$ and $2\theta \approx 56°$, while the peaks at $2\theta \approx 12°$ and $2\theta \approx 60°$ disappeared. These peaks correspond to the Ramsdellite-type structure (R-MnO_2) having orthorhombic symmetry and a *Pnma* space group. Therefore, a phase transformation process from α to R-MnO_2 occurred. A deeper analysis to quantify the lattice parameter Rietveld Refinement was carried out and the results are presented in Table 1. Lattice parameter data show that the b lattice changed from the initial 9.8338 ÅÅ for $x = 0.10$ to 4.4708 Å for $x = 0.15$, and this is confirmation of the transformation of α to R-MnO_2.

Additionally, it was shown that for the Fe-doped samples, the intensities of the diffraction peaks were reduced, accompanied by a broadening of the observed peaks. This confirms that the substitution of Fe ions for the Mn ions at the octahedron site could degrade the crystallinity of MnO_2. Accordingly, some amount of strain along with the vacancy defects is generated. The crystallite sizes (D) and micro-strain (ε) of all the samples were estimated using MAUD software.[29] The goodness of fit was determined by the reliability parameter R_{wp} and is shown in Table 2. Meanwhile the dislocation density (δ) represents the amount of defects present in the samples, and this is defined as the length of dislocation lines per unit volume of the crystal and was calculated using the equation,[30]

$$\delta = \frac{1}{D^2} \quad (1)$$

where D is the crystallite size.

It is clear from Table 2 that there is a decrease in crystallite size and an increase in the lattice micro-strain and dislocation density in the α-MnO_2 phase ($x = 0$–0.10). This indicates that Fe substituted Mn inside octahedral MnO_6 leads to more defects in the samples. The high lattice strain values cause a phase change in MnO_2, as indicated by the significant drop in micro-strain, ε, and a significant increase in the dislocation density, δ. Furthermore, by considering the Fe^{3+} radius is larger than that of Mn^{4+}, and the instability of the local charge when 3+ of Fe substitutes 4+ of Mn (Fe'_{Mn}), which is possibly accommodated

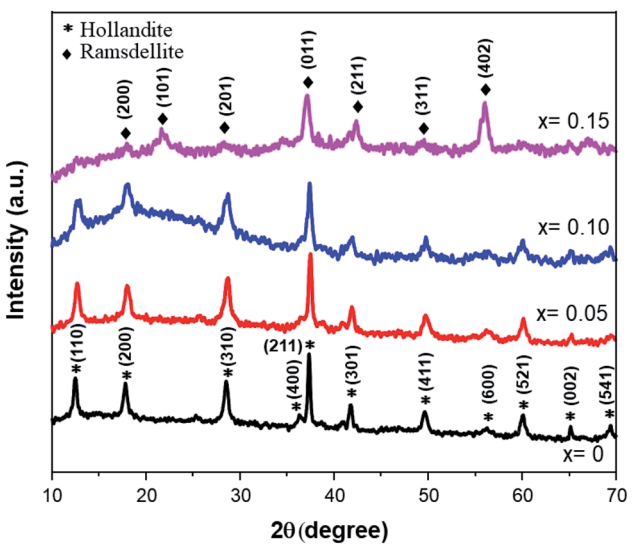

Fig. 2 The XRD patterns of Fe-doped MnO_2 samples, $Mn_{1-x}Fe_xO_2$.

Table 1 The lattice parameters of the Fe-doped MnO_2 samples, $Mn_{1-x}Fe_xO_2$

	Reliability factor				Lattice parameters			
Sample	R_{wp}	R_B	R_{exp}	GOF	a	b	c	Crystal symmetry
$x = 0$	6.77	1.89	5.69	1.41	9.8614(6)	9.8614(6)	2.8686(4)	$I4/m$
$x = 0.05$	5.83	1.48	4.93	1.39	9.8326(2)	9.8326(2)	2.8632(9)	$I4/m$
$x = 0.10$	6.16	1.20	5.46	1.27	9.8338(5)	9.8338(5)	2.8705(9)	$I4/m$
$x = 0.15$	5.45	2.72	4.68	1.35	9.6716(3)	4.4708(9)	2.8095(2)	$Pnma$

Table 2 Crystallite size (D), micro-strain (ε) and dislocation density (δ) of the $Mn_{1-x}Fe_xO_2$ samples

Sample	D (nm)	ε ($\times 10^{-3}$)	δ (lines per nm^2) $\times 10^{-4}$	R_{wp} (%)
$x = 0$	49.06	2.66	4.15	7.079
$x = 0.05$	23.05	4.39	18.82	6.257
$x = 0.10$	16.18	4.92	35.43	6.653
$x = 0.15$	5.47	0.25	334.21	5.657

by the oxygen vacancy ($V_O^{\bullet\bullet}$), after 0.15Fe is inserted into the Mn site, then the octahedron chains are broken from the (2 × 2) to (2 × 1) tunnels, and this is illustrated in Fig. 3 and was visualized with the VESTA software.[31] There are possible effects when Fe^{3+} dissolves in MnO_2, causing a decrease in the crystalline size, and these include an increase in the size of the octahedron and oxygen vacancy $V_O^{\bullet\bullet}$ creation following the defect reaction. This can be represented using Kroger–Vink notation:

$$Fe_2O_3 \xrightarrow{MnO_2} 2Fe'_{Mn} + V_O^{\bullet\bullet} + 3O_O^{\times} \quad (2)$$

The infrared characterization interactions among the ions/molecules of the surfaces with the nanostructures cause alterations in the vibrational frequencies compared to isolated molecules or pure nanostructures. Fig. 4 shows the FTIR spectra of MnO_2 and Fe-doped samples. The high-frequency modes around 466 and 522 cm^{-1} represent the stretching vibration of Mn–O. Meanwhile, the mode at 711 cm^{-1} can be ascribed to the Mn–O–Mn stretching vibration, further supporting the formation of octahedral MnO_6. The displacement of oxygen anions relative to the Mn cations along the direction of the octahedral chain produces peaks at 522 cm^{-1}. Furthermore, an increase in Fe-doping in the sample affects the transmittance intensities of 466, 522, and 711 cm^{-1} being reduced.

Peaks at ≈1545 cm^{-1} are attributed to the vibrations of Mn–O–H bonds.[32] A decrease in the intensity at this frequency for the doped sample indicates that oxygen vacancies are present in the Fe-doped sample. Moreover, a broad band at 3400–3500 cm^{-1} is assigned to the stretching vibration of O–H. These hydroxyl groups originate from water adsorbed onto the surface of the MnO_2 samples. The presence of more water adsorbed in a sample with Fe-doping indicates that an amount of water is slightly accumulated in the tunnel of Fe-doped MnO_2.[23] Additionally, small peaks at 2851 cm^{-1} and 2921 cm^{-1} are attributed to C–H stretching and bending vibrations of ethanol,[33] which was present after the washing process (Table 3).

The vibrational lattice features of the RS spectroscopy data provide a reliable description of different local structural as well as crystalline disorders or defects of the MnO_2 related compound.[30] Considering the XRD analysis, α-MnO_2 has a body-centered tetragonal structure with space group $I4/m$, and the RS spectroscopy factor group analysis indicates that MnO_2 will be assigned as 15 spectroscopic modes of $6A_g + 6B_g + 3E_g$. However, it might be difficult to observe these Raman-active modes in the polycrystalline samples due to the low polarizabilities of some of these modes and the overlap of incompletely resolved

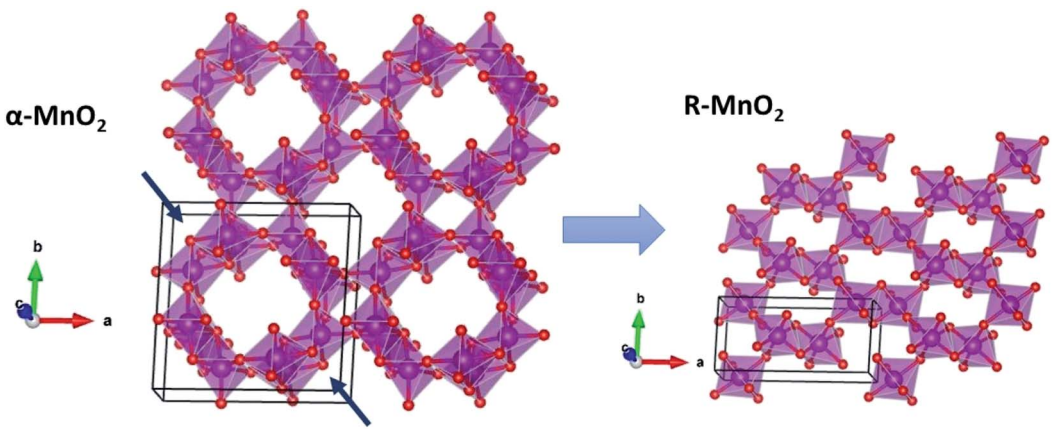

Fig. 3 Phase transformation of α-MnO_2 to R-MnO_2 structure.

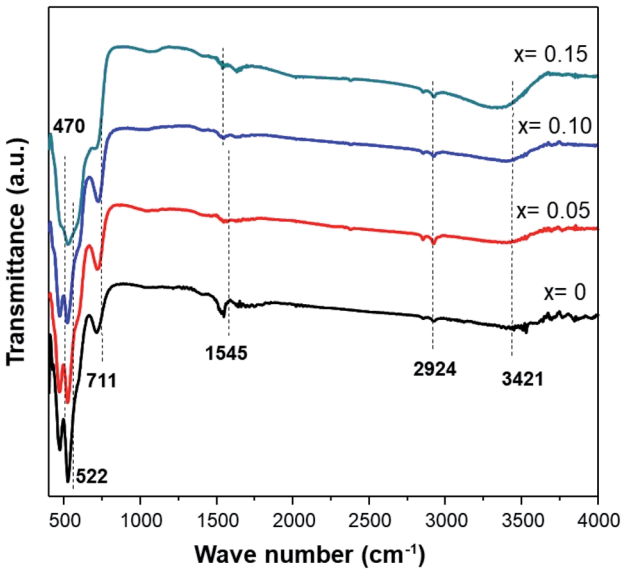

Fig. 4 FTIR spectra of the Fe-doped MnO_2 samples, $Mn_{1-x}Fe_xO_2$.

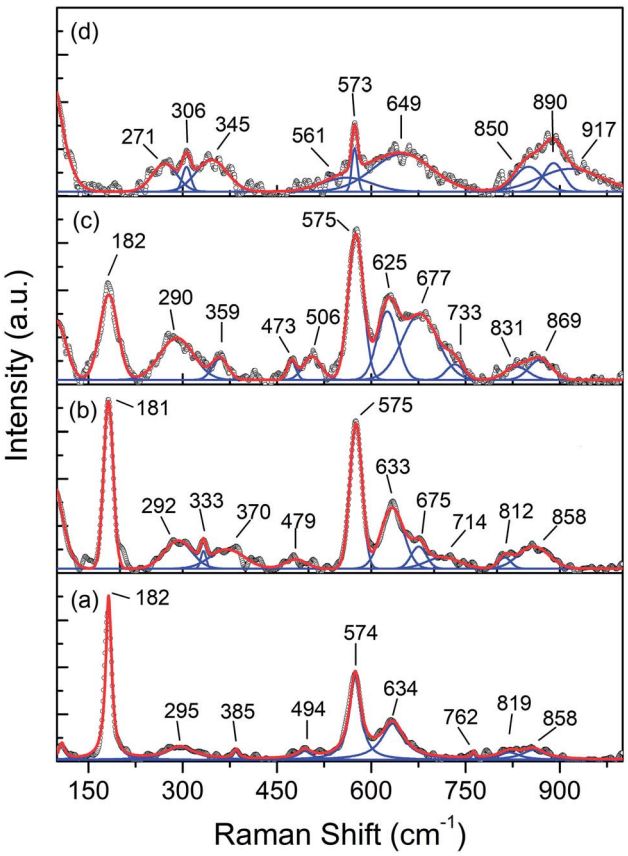

Fig. 5 Raman spectra of Fe-doped MnO_2 samples, $Mn_{1-x}Fe_xO_2$. (a) $x = 0$; (b) $x = 0.05$; (c) $x = 0.10$; and (d) $x = 0.15$.

modes.[34] In these samples, the Raman scattering is characterized by three sharp peaks at about 181, 574, and 634 cm^{-1}, as well as six weak bands recorded at 295, 385, 494, 762, 819, and 858 cm^{-1} that be indexed to α-MnO_2, as designated in Fig. 4a. Two Raman bands at 181 and 385 cm^{-1} are assigned to E_g symmetry, while those at 494 and 674 cm^{-1} are assigned to B_g symmetry, and three bands at the high-frequency regions of 574, 634, and 762 cm^{-1} are ascribed to symmetrical Mn–O vibrations and are assigned to A_g symmetry. Considering the crystalline structure of α-MnO_2 (Fig. 2), the basic MnO_6 octahedron shared edges and corners build a (2 × 2) tunnel space. Hence, important vibrational interactions are expected to arise, along with interactions perpendicular to the O–Mn–O–Mn–O chains.

Fig. 5 depicts the Raman absorption spectroscopy data, where a low-frequency Raman band at 181 cm^{-1} is assigned to an external vibration that is derived from the translational motion of the MnO_6 octahedral structure, which is concerned with the existence of tunnel ions.[2] The weak peaks at 295, 385, 494, 762, 819, and 858 cm^{-1} reveal the phonon density of states rather than the Raman-allowed zone center phonons, and this is due to the confinement of phonons by crystal defects and local lattice distortions in the as-prepared MnO_2 nanowires.[35] A band at 634 cm^{-1} can be attributed to the symmetric stretching of O–Mn–O vibrations, perpendicular to the direction of the MnO_6 octahedral double chains. Meanwhile, the peak at 574 cm^{-1} corresponds to the vibrations of the O–Mn–O–Mn chains in the octahedral planes. Therefore, the Raman band observed in this range is attributed to the displacement of the oxygen atoms relative to the manganese atoms along the octahedral chains.

Doping Fe into MnO_2 causes variation in the intensity peaks of the Raman bands due to the confinement of phonons by crystal defects and local lattice distortions. From Fig. 5(b and c),

Table 3 Peak assignments on the FTIR spectra of $Mn_{1-x}Fe_xO_2$

FT-IR peaks (cm^{-1})				Vibrational mode
$x = 0$	$x = 0.05$	$x = 0.10$	$x = 0.15$	
470.65	466.79	468.72	—	Stretching vibration Mn–O
522.73	520.8	518.87	524.66	Stretching vibration Mn–O
711.76	713.69	721.40	702.11	Stretching vibration Mn–O–Mn
1545.03	1537.32	1545.03	1529.6	Vibrations of O–H combined with Mn
2924.18	2920.32	2922.25	2922.25	Stretching vibration C–H
3421.83	3367.82	3396.76	3304.17	O–H stretching vibration of surface water

it can be observed that with Fe-doping ($x = 0.05$ and $x = 0.10$), the Raman peak around 630 cm^{-1} strengthens. This indicates that some lattice rearrangements have occurred without a structural phase transition. An increase in intensity around 574 cm^{-1} signifies an increase in the distortions associated with oxygen displacement and the number of oxygen vacancies with doping.

The greater Fe-doped sample ($x = 0.15$), displayed in Fig. 4d, shows a significant change in the Raman peak, which explains the phase change from α-MnO_2 to R-MnO_2 as presented by the XRD results. Ramsdellite MnO_2 indicates 18 Raman modes of activity such as $6A_{1g} + 3B_{1g} + 6B_{2g} + 3B_{3g}$.[36] The Raman spectrum of the $x = 0.15$ sample displays two main sharp peaks at 573 and 649 cm^{-1} and two weak peaks recorded at 271 and 345 cm^{-1}. The two sharp peaks are assigned to an A_{1g} spectroscopic and indicative well-developed orthorhombic structure with an interstitial space consisting of (1×2) channels.[37] In addition, the peak at 181 cm^{-1} disappears, and this indicates the reduction of cations in the tunnel.

The Raman bands at 800–900 cm^{-1} initially have a very low intensity for $x = 0$, and this increases for a higher x value, in particular for $x = 0.15$. Considering that the oxidation state of the Fe dopant is smaller than Mn, the oxygen vacancy formation due to the dopants increases parallel to the Fe-doped content. Therefore, the Raman bands at 800–900 cm^{-1} can be attributed to oxygen vacancies and the increase in its intensity relates to vacancy concentration.[38] Moreover, the presence of an Fe–O vibration in Fe-doped MnO_2, as shown in Fig. 5(b–d), was identified as a mixture of α and γ phases of Fe_2O_3 and magnetite (Fe_3O_4). The band at 333 cm^{-1} can be attributed to E_g modes of α-Fe_2O_3, while γ-Fe_2O_3 is shown at around 359 (E_g), 370 (E_g), 506 (T_{2g}), and 714 (A_{1g}) cm^{-1}.[39] Some of the Fe_3O_4 peaks are assigned to symmetry $E_g \approx 306$ cm^{-1}, $T_{2g} \approx 479$, ≈ 561 cm^{-1}, and $A_{1g} \approx 675$ cm^{-1}.

In order to deeply explore the information concerning the chemical state and composition of the samples, X-ray photoelectron spectroscopy (XPS) was carried out. The XPS survey spectra in Fig. 6 reveals that the samples consist of Mn and O elements with a slight number of K cations and Fe elements. Furthermore, each sample shows carbon as a contaminant.

The detailed analysis of the XPS spectra of the $Mn_{1-x}Fe_xO_2$ samples is given in Fig. 7 and 8. In the Mn 2p spectrum (Fig. 7a), two spin–orbit doublets of Mn $2p_{3/2}$ and Mn $2p_{1/2}$ are detected. For $x = 0$, at 641.69 and 653.60 eV with a binding energy gap of 11.91 eV, the spectrum indicates the existence of MnO_2. Meanwhile, the binding energies for $x = 0.05$ are 641.66 eV (Mn $2p_{3/2}$) and 653.45 eV (Mn $2p_{1/2}$) with a binding energy gap of 11.58 eV, so they are close to those of the MnO_2 sample. In contrast, for $x = 0.15$, the peak positions for Mn $2p_{3/2}$ (640.25 eV) and Mn $2p_{1/2}$ (652.03 eV) with a binding energy gap of 11.74 eV, are shifted to lower binding energies compared to those for MnO_2. Jain (2019)[40] reported that the binding energy shifts to a lower value related to the decreasing oxidation state of Mn in the oxide ($MnO_2 > Mn_2O_3 > Mn_3O_4$). Therefore, the shift to lower energy for the $x = 0.15$ sample was interpreted as evidence for a mixed $Mn^{2+/3+}$ state.[41]

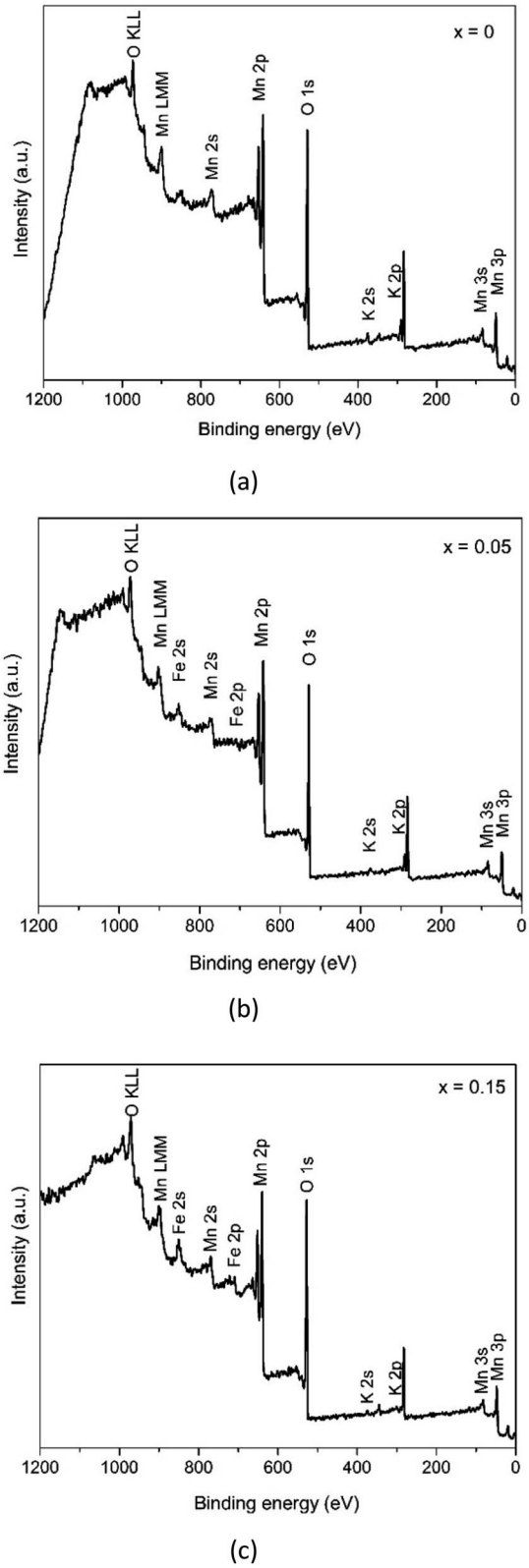

Fig. 6 XPS survey spectra of $Mn_{1-x}Fe_xO_2$.

Following a deconvolution process using the Lorentzian function, four peaks located at 641.63, 642.85, 652.99, and 653.96 eV were obtained for the MnO_2 2p spectra, while those for the other samples are depicted in Table 4. These peaks were

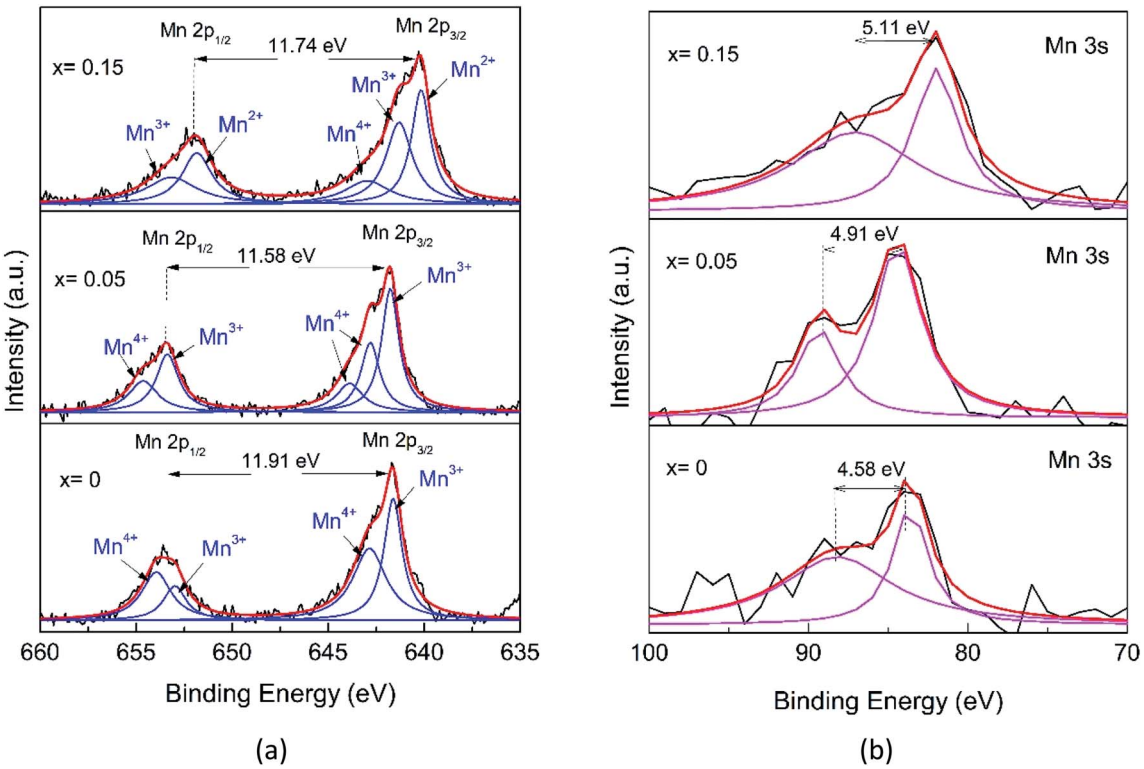

Fig. 7 XPS spectra of (a) Mn 2p, and (b) Mn 3s for the $Mn_{1-x}Fe_xO_2$ samples.

assigned to the Mn^{3+} ($2p_{3/2}$), Mn^{4+} ($2p_{3/2}$), Mn^{3+} ($2p_{1/2}$), and Mn^{4+} ($2p_{1/2}$) species, respectively. The presence of two chemical environments for Mn^{4+} could be ascribed to the bulk MnO_6 octahedron (O–Mn–O) and the surface environment that could present the O–Mn–OH structure. An amount of Mn^{3+} could also be present, probably due to the cations inside the tunnel, which can induce the reduction of Mn^{4+} to Mn^{3+} to maintain charge neutrality and the oxygen vacancies that could also contribute to Mn^{3+} formation.[42] With greater Fe-ion doping (0.15), the special shapes of the peak of Mn 2p represent the existence of Mn in a mixture of various valence states, including Mn^{2+}, Mn^{3+}, and Mn^{4+}. The components located at 642.97 and 653.17 eV are ascribed to Mn^{4+}. The components located at 641.31 and 651.84 eV are attributed to Mn^{3+} and a minor component of Mn^{2+} at 640.17 eV.

However, due to the overlap in binding energy values, the complex multiplet splitting, the satellite-loss features, and the asymmetry of the spectra,[43] it is difficult to determine the valence of Mn from the Mn 2p peaks alone. Further analysis of the Mn 3s doublet splitting (ΔE_{3s}) offers a detailed understanding of the Mn chemical state (Fig. 7b). The Mn 3s peak splitting is caused by the electron exchange in the 3s–3d orbitals of Mn upon photoelectron ejection, which is more sensitive to the oxidation state of manganese than that of Mn 2p.[44] For convenience, the estimation of the AOS (average oxidation state) for Mn from ΔE_{3s} was calculated using the following equation,[41]

$$AOS_{Mn} = 9.67 - 1.27\Delta E_{3s} \quad (3)$$

The AOS numbers of Mn are listed in Table 4. These decrease with x, showing more influence of the Mn^{3+} characteristics and the values are consistent with the Mn 2p analysis, indicating the existent of Mn^{2+} for $x = 0.15$. Interestingly, there are no extra peaks in the XRD pattern of α-MnO_2 (Fig. 2), indicating that the oxidation state of Mn is 4+. However, the XPS data of the Mn 2p spectra for α-MnO_2 (Fig. 7a) show a distinct presence of Mn^{3+}, but the existence of Mn^{3+} may not be due to the presence of Mn_2O_3. These observations indicate that Mn^{3+} is possibly localized on the surface of α-MnO_2 without the formation of lower oxides.[40] Or, Mn^{3+} is compensated by the oxygen vacancy. Furthermore, by increasing the amount of Fe-doping ($x = 0.15$), the structure transforms to Ramsdellite from the initial α-MnO_2. This indicates a structural distortion in the Ramsdellite structure, and this is caused by an interaction of Jahn–Teller distortion of the octahedrally coordinated $Mn^{3+}O_6$.[15]

Fig. 8a shows the O 1s core-level XPS spectrum. The O 1s XPS spectra for $x = 0$ and $x = 0.05$ are deconvoluted into three peaks, which can be assigned to Mn–O–Mn (~529.28 eV), Mn–O–H (~530.55 eV), related to the oxygens from bulk MnO_6, and surface Mn–O–H, respectively, in agreement with the presence of two Mn chemical environments.[42] However, the major O 1s peak for $x = 0.15$ shifts to a lower level and decreases in intensity, indicating a change in the Mn–O coordination configuration, probably due to the formation of the Fe–O–Mn bond.

Further analysis of the Fe 2p spectra of the $x = 0.05$ samples, despite the data being scattered (Fig. 8b), shows broad peaks. The characteristic Fe spin–orbit peaks of the $x = 0.05$ sample

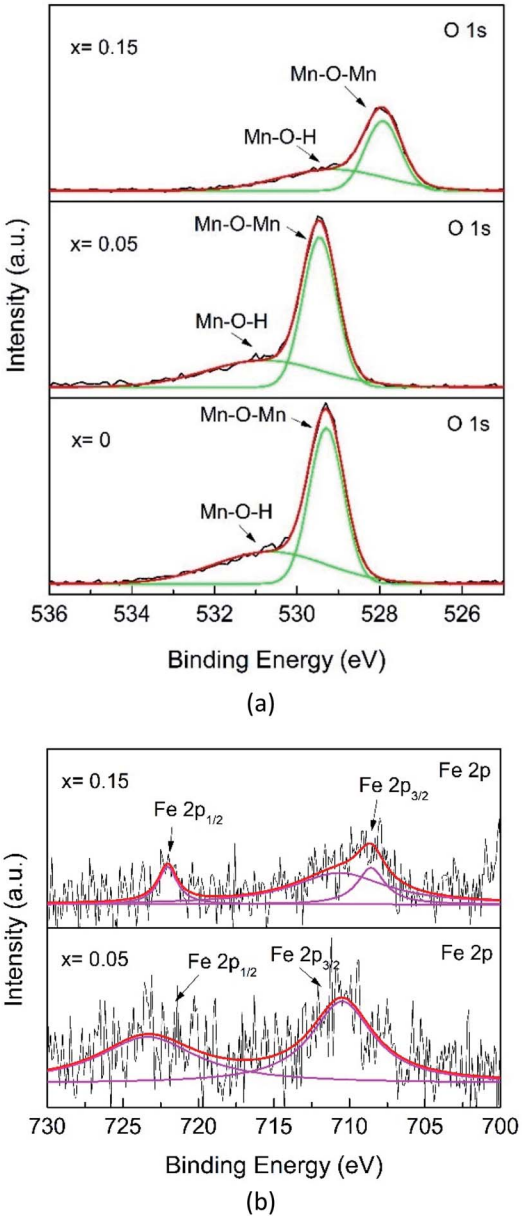

Fig. 8 XPS spectra for (a) O 1s and (b) Fe 2p of the $Mn_{1-x}Fe_xO_2$ samples.

$2p_{1/2}$ is located at 723.36 eV, indicating the existence of a mixture of Fe^{2+} and Fe^{3+}, while Fe $2p_{3/2}$ is located at 710.49 eV for Fe^{4+}. However, for $x = 0.15$, the Fe $2p_{1/2}$ spectrum exhibits lower binding energies, located at 722.04 eV and $2p_{3/2}$ is located at 708.58 eV, and this can be interpreted as a mixture of Fe^{2+} and Fe^{3+}, while the peak at 710.66 eV was for Fe^{4+}.[45] Recalling the XRD pattern (Fig. 2), no compound containing Fe species could be observed, indicating that Fe has substituted with Mn. As mentioned before, the Fe element present in the XPS spectrum also reveals that Fe-doping plays a key role in phase transformation.

In order to determine the electronic and structural properties of the MnO_2 and Fe-doped samples, X-ray absorption fine structure (XAFS), as well as X-ray absorption near edge structure (XANES) and extended X-ray absorption fine structure (EXAFS) spectroscopies were performed. XANES can provide information on the electronic structure of Mn present in the different oxides, especially for the short-range order. The Mn K-edge XANES spectra of the prepared samples are presented in Fig. 9a, and the reference compositions of MnO_2, Mn_2O_3, and MnO_2 are also included.

Table 4 The XPS data for Mn 2p and Mn 3s values of $Mn_{1-x}Fe_xO_2$

	Mn 2p			Mn 3s	
Samples	Species	Peak (eV)	Area (%)	ΔE_{3s}	AOS
$x = 0$	$2p_{3/2}$ (Mn^{3+})	641.629	44.11	4.58	3.86
	$2p_{1/2}$ (Mn^{3+})	652.99			
	$2p_{3/2}$ (Mn^{4+})	642.854	55.89		
	$2p_{1/2}$ (Mn^{4+})	653.958			
$x = 0.05$	$2p_{3/2}$ (Mn^{3+})	641.776	53.54	4.91	3.43
	$2p_{1/2}$ (Mn^{3+})	653.380			
	$2p_{3/2}$ (Mn^{4+})	642.811	46.46		
	$2p_{3/2}$ (Mn^{4+})	643.886			
	$2p_{1/2}$ (Mn^{4+})	654.635			
$x = 0.15$	$2p_{3/2}$ (Mn^{2+})	640.174	26.35	5.11	3.18
	$2p_{3/2}$ (Mn^{3+})	641.312	44.49		
	$2p_{1/2}$ (Mn^{3+})	651.844			
	$2p_{3/2}$ (Mn^{4+})	642.971	29.16		
	$2p_{1/2}$ (Mn^{4+})	653.171			

It can be seen that the shapes of all the samples and the peak positions are similar to each other. The absorption edges are slightly shifted towards lower energy with increasing Fe-doped concentration, and this can be attributed to the chemical shift effect. The absorption edge shift to lower energy with increasing Fe-dopant could be used to obtain an average oxidation state of absorbent through the first derivatives of the edge curves. The absorption edge energies of $Mn_{1-x}Fe_xO_2$ are determined to be 6552 eV, 6551.5 eV, 6551 eV and 6549.4 eV for $x = 0$, 0.05, 0.10 and 0.15, respectively. The Mn K-edge absorption energies of the reference materials were 6544.21 eV (MnO), 6548.25 eV (Mn_2O_3), and 6552.4 eV (MnO_2). The absorption edges of all the samples were lower than those of the MnO_2 (Mn^{4+}) reference. Increasing the x value leads to the gradual shift of the absorption edge towards Mn_2O_3 (Mn^{3+}). This is an indication that the Mn absorber possesses a mixture of oxidation states, namely 3+ and 4+. The average oxidation state (AOS) of Mn was determined by establishing a linear relationship between the Mn K-edge energy and the Mn oxidation state (Fig. 9b).

According to the Fe K-edge XANES spectra (Fig. 10a), the absorption energy (E_0) of the Fe-doped samples with $x = 0.05$–0.15 observed a slight shift to higher energy, compared with the Fe_2O_3 standard. The absorption energy of $x = 0$ was 7123.79 eV, and this gradually shifted to that of the Fe_2O_3 standard (7123 eV) at higher x values (0.10 and 0.15), with values of 7123.48 eV and 7123.25 eV. This shift indicates that the average oxidation state of Fe is between 3+ and 4+ (Fig. 10b). The mixed oxidation states of the Mn and Fe results confirms the XPS analysis results described previously.

EXAFS studies the local structure information. Fig. 11 shows the curve-fitting Fourier transform (FT) into R-space. The fitting

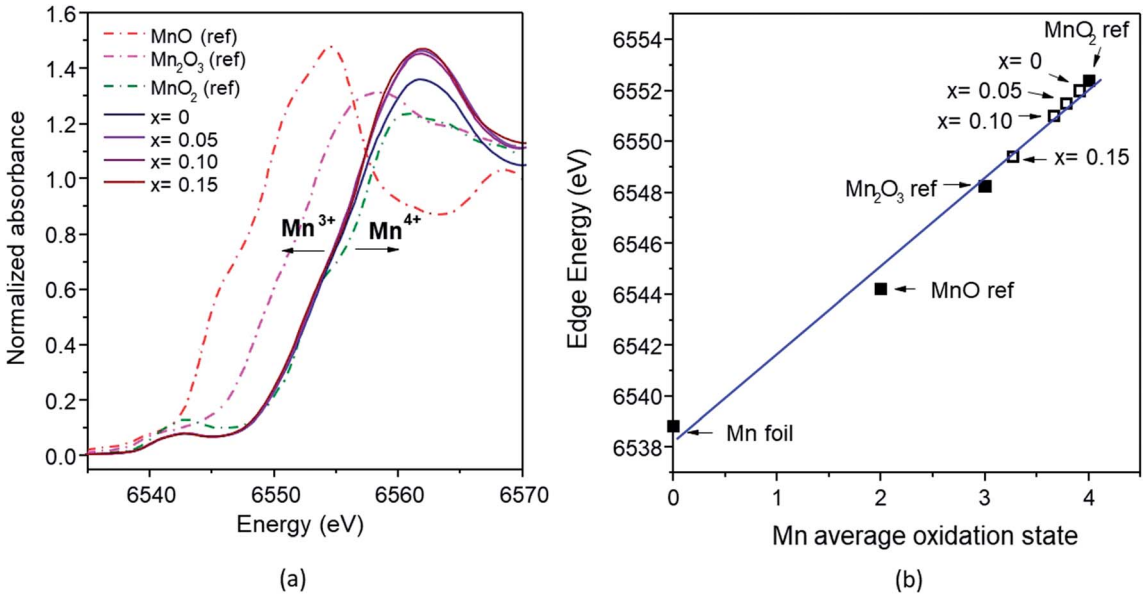

Fig. 9 (a) Mn K-edge XANES spectra of the MnO_x reference and $Mn_{1-x}Fe_xO_2$ samples; (b) average oxidation states of Mn for the reference and samples derived from the K-edge energies.

process meant that the interatomic distances (d) and the Debye–Waller factors (σ) were left as free parameters, and the coordination number (CN) was fixed. The results of the curve fitting are summarized in Table 5. The α-MnO_2 reference exhibits a first shell Mn–O interaction distance of around 1.8692 Å, and the second and third shells associated with the characteristic Mn–Mn_{es} (es = edge-shared) and Mn–Mn_{cs} (cs = corner shared) distances were around 2.8979 Å and 3.4248 Å, respectively. It was observed that the interatomic distances of Fe-doped MnO_2 were slightly different to those of the MnO_2 standards.

The distance of the Mn–O bond shifts toward larger R values in line with the doping percentage. The Mn–O distribution peak intensity exhibited a small increase with increasing Fe content ($x > 0$), suggesting that the Fe neighboring structure of Mn–O had changed in its Mn oxidation state from 3+ to 4+.[21] However, the opposite occurred for the undoped MnO_2 sample.

The interatomic distances of the Mn–Mn_{es} octahedra initially showed smaller and shorter values for the $x = 0$–0.10 samples, and increased values for $x = 0.15$. The increasing peak intensity for the doped sample, in the Mn–Mn_{es} shell, is probably due to the higher mean coordination number of Mn at the second cationic coordination shell.[6] However, the opposite trend is observed for the Mn–Mn_{cs} octahedra. The intensity of the FT peaks significantly decreased for higher Fe content,

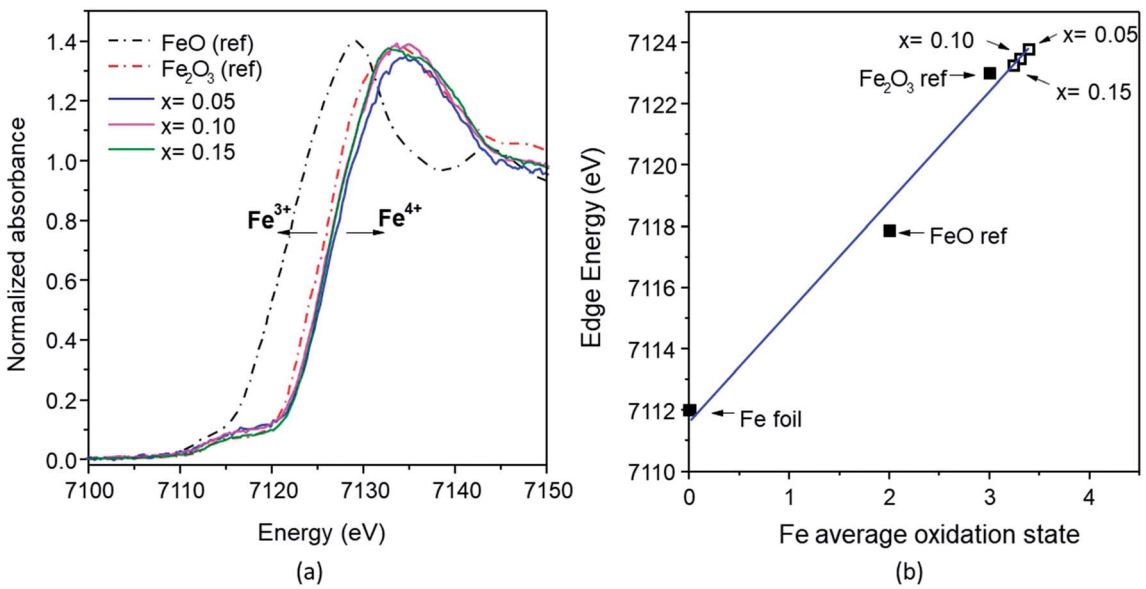

Fig. 10 (a) Fe K-edges XANES spectra of the FeO_x reference and $Mn_{1-x}Fe_xO_2$ samples; (b) average oxidation states of Fe for the reference and samples derived from the K-edge energies.

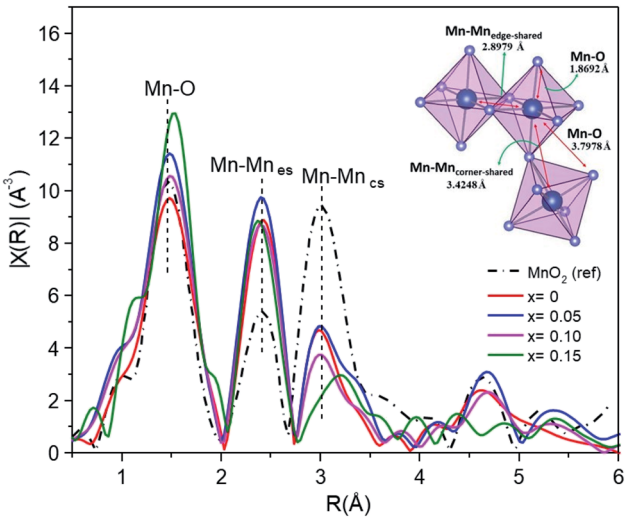

Fig. 11 Fourier transform magnitudes of the EXAFS spectra for the $Mn_{1-x}Fe_xO_2$ samples.

Table 5 Interatomic distances of the Mn core atom to the first neighbor O octahedron, second neighbor Mn, and third neighbor Mn and O for the MnO_2 reference and $Mn_{1-x}Fe_xO_2$ samples

Sample	Shell	R (Å)	σ^2	R-Factor (%)
MnO_2 (ref)	Mn–O	1.8692	0.00344	1.997
	Mn–Mn	2.8979	0.00801	
	Mn–Mn	3.4248	0.00001	
	Mn–O	3.7978	0.01564	
$x = 0$	Mn–O	1.8815	0.00430	2.325
	Mn–Mn	2.8750	0.00403	
	Mn–Mn	3.4365	0.00531	
	Mn–O	3.0907	0.04445	
$x = 0.05$	Mn–O	1.8797	0.00270	2.038
	Mn–Mn	2.8737	0.00329	
	Mn–Mn	3.4348	0.04918	
	Mn–O	3.1028	0.00455	
$x = 0.10$	Mn–O	1.8884	0.00342	2.121
	Mn–Mn	2.8853	0.00418	
	Mn–Mn	3.4426	0.00591	
	Mn–O	3.5274	0.01559	
$x = 0.15$	Mn–O	1.8949	0.00005	2.575
	Mn–Mn	2.9600	0.00111	
	Mn–Mn	2.8966	0.00756	
	Mn–O	3.5777	0.01993	

revealing that the increased structural distortion is due to the insertion of K in the tunnel, Fe substitution into the α-MnO_2 structure and an increased amount of Mn^{3+} ions, as indicated by the XPS and XANES analysis, showing active Jahn–Teller distortion. Furthermore, there is a significant broadening and reduction of the peak intensity and notably different FT peak features of the high Fe-doped ($x = 0.15$) sample for Mn–Mn_{cs}. This difference is likely due to the severe Jahn–Teller distortion in the corner-shared MnO_6 octahedra, and the breakage of the tunnel structure becomes (2 × 1).[46]

On the other hand, the Mn–Mn_{cs} bond length increases slightly with the concentration of Fe. The lengthening of the Mn–Mn_{cs} bond can occur because of the reduction of Mn^{4+} to Mn^{3+}. As the ionic radius of the manganese cation increases ($Mn^{4+} \rightarrow Mn^{3+}$) and the Jahn–Teller effect becomes active, Mn^{3+} can distort the structure and lengthen the Mn–Mn_{cs} bond.[47] This fact is similarly consistent with the mean oxidation state of Mn, which is lower than 4+, as determined by XPS and XANES in $Mn_{1-x}Fe_xO_2$.

The morphologies and microstructures of MnO_2 with different doping Fe^{3+} concentrations were examined using scanning electron microscopy (SEM). One-dimensional MnO_2 nanorods were typically synthesized in the $Mn_{1-x}Fe_xO_2$ samples with x = 0–0.10, as shown in Fig. 12a–c. However, α-MnO_2 (Fig. 12a and b) shows a rod-like morphology with an average diameter of about 70 nm and a length of about 2 μm. The rods are uniform throughout their entire length.

This rod-like morphology implies anisotropic growth of the nanocrystals. The length of the aligned nanowires decreased with increasing Fe^{3+} concentration. MnO_2 combined with very short nanorods were shown in the sample with $x = 0.10$ Fe content (Fig. 12c). The morphology of the sample of MnO_2 doped with Fe ($x = 0.15$), which is characteristic of R-MnO_2, is shown in Fig. 12d. It can be seen that the formation of clusters with plate-like and rod-like nanosized crystallites, which both belong to MnO_2, may be due to the growth of newly formed MnO_2 colloids during early formation. The amount of these plate-like crystallites is low.

Table 6 provides the EDS analysis of MnO_2, and reveals that the sample is composed of O, Mn, and K. The presence of K ions (about 2%) indicates that K^+ could simultaneously occupy the structure channels (2 × 2) and stabilize the hollandite structure type. By incorporating K^+ ions into the tunnel, a state of charge neutrality is maintained in the structure by reducing Mn^{4+} to Mn^{3+}.[48] This confirms the structural distortion in the $Mn_{1-x}Fe_xO_2$ sample with $x = 0$. Moreover, small amounts of Fe element are confirmed in the EDS table. Increasing the x values of Fe-doping causes a reduced number of K^+ ions. This is consistent with the phase change from α-MnO_2 (2 × 2) to R-MnO_2 (2 × 1). The evidence of successful Fe-doping could be verified through XPS.

To obtain deep insight into the morphology features and crystal structures of the Fe-doped MnO_2 samples, $Mn_{1-x}Fe_xO_2$, TEM, HRTEM, and SAED characterizations were used for analysis. The morphologies of all the samples, displayed in Fig. 13(a, f and k), clearly show the shape of the MnO_2 nanorods, and this corresponds to the SEM morphology shown in Fig. 12. The TEM image of α-MnO_2, with $x = 0$, (Fig. 13a), shows the presence of nanorods with a diameter of 20–80 nm. Fig. 13(b) indicates the single crystalline characteristic of the α-MnO_2 nanorod, as affirmed by comparing with the SAED pattern in Fig. 13(d), which can be indexed to (200), (110), and (411). The growth direction of the nanotubes is at [001]. Fig. 13(c) shows the lattice fringe with d-spacing of 0.56 nm, corresponding to the d value of the (200) plane of α-MnO_2, and this relates well with the XRD data shown in Fig. 2(a). The illustration of the crystal plane (200) is shown in Fig. 13(e).

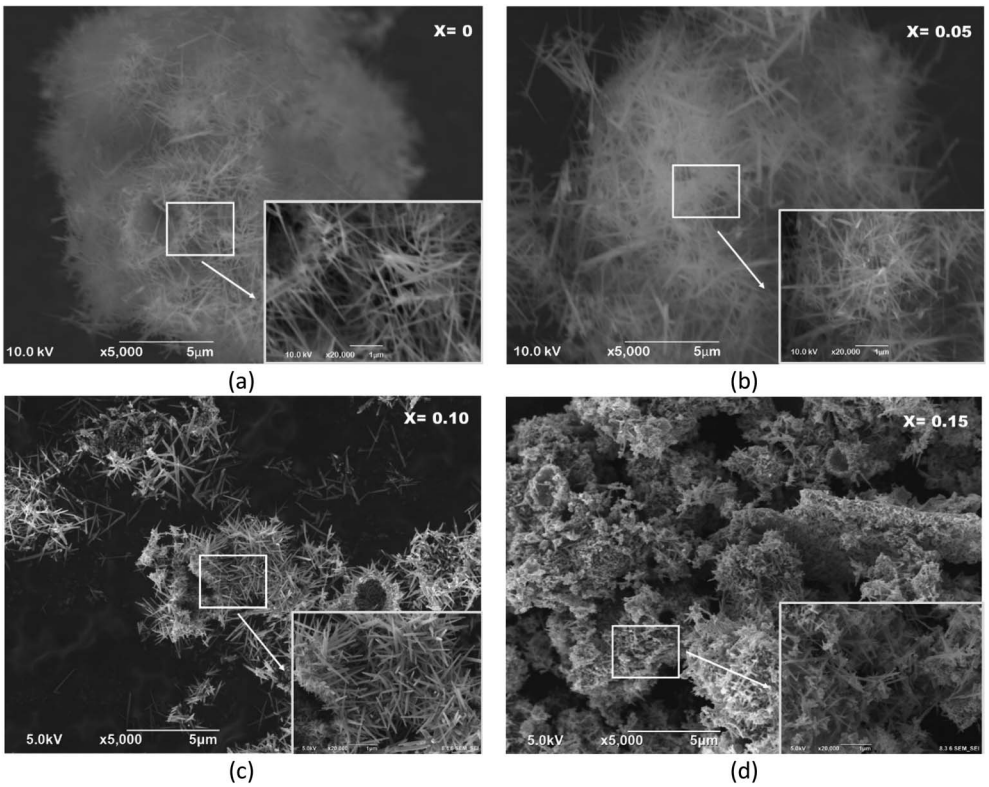

Fig. 12 SEM images of $Mn_{1-x}Fe_xO_2$, (a) $x = 0$; (b) $x = 0.05$; (c) $x = 0.10$; and (d) $x = 0.15$ showing the morphology of the nanorods; inset: the magnification of 20 000×.

Table 6 EDS analysis of the element percentage of the $Mn_{1-x}Fe_xO_2$ samples

	Atomic (%)			
Element	$x = 0$	$x = 0.05$	$x = 0.10$	$x = 0.15$
O–K	77.22	76.86	64.73	66.60
Mn–K	20.63	19.86	29.90	28.05
K–K	2.15	1.93	2.38	1.25
Fe–K	—	1.35	2.95	4.10

The addition of Fe ($x = 0.05$–0.10) affects the morphology of the $Mn_{1-x}Fe_xO_2$ samples. The average thickness of the nanorods varies from 50 to 100 nm. The HRTEM images in Fig. 13(g and l) clearly show the disordered orientation of the sample. Correspondingly, the exposed plane of the nanorods in the Fe-doped samples ($x = 0.05$–0.10) and its lattice are shown in Fig. 13(g and h)–(l and m) for $x = 0.05$ and 0.10, respectively. The d value of the lattice fringes (≈ 0.67 nm) relates to the (110) plane of α-MnO_2 and indicates that the growth direction of the nanorod is at [001]. This plane is consistent with the SAED data in Fig. 13(i and n). Fig. 13(p) shows the different morphology of the $x = 0.15$ sample. The average length of the nanorods is reduced, while the thickness is around 70 nm. This morphology is related to the R-MnO_2 phase and is shown in the FESEM image in Fig. 12(d). The schematic model of the R-MnO_2 nanorods in Fig. 13(r) shows that the interplanar distance of the (200) crystal planes is enlarged from d-spacing to 0.52 nm. The SAED pattern (Fig. 13(s)) shows the lattice fringe matches with the (111), (200), and (131) crystal planes that confirm the diffraction pattern of orthorhombic R-MnO_2.

3.3. Electrical characterization/analysis

The electrical properties of the $Mn_{1-x}Fe_xO_2$ samples were investigated using a complex impedance technique. This technique is principally used for characterizing electrical properties, including the determination of ionic conductivity, capacitance, permittivity, and the dielectric constant. The plots of imaginary impedance (Z'') *versus* real impedance (Z') (Nyquist plot) for different Fe-doped samples ($x = 0$–0.15) are shown in Fig. 14. The addition of Fe-doping causes an increase in the radius of the semicircles. One small semicircle was seen for $x = 0$–0.05, suggesting that the electrical processes in the material arise due to the contribution from grain material. Furthermore, the inductance response observed at high frequency relates to the wiring system. When $x = 0.10$–0.15, there are two overlapping semicircles, corresponding to the grain (semicircle at high frequencies) and grain boundaries (low-frequency semicircles).

The impedance data has been linked to the equivalent circuits (inset in Fig. 14), which consist of the inductance from wires (L), the wire shunt resistance (R_s), and the inside series combination of grain and grain boundaries. The first consists of

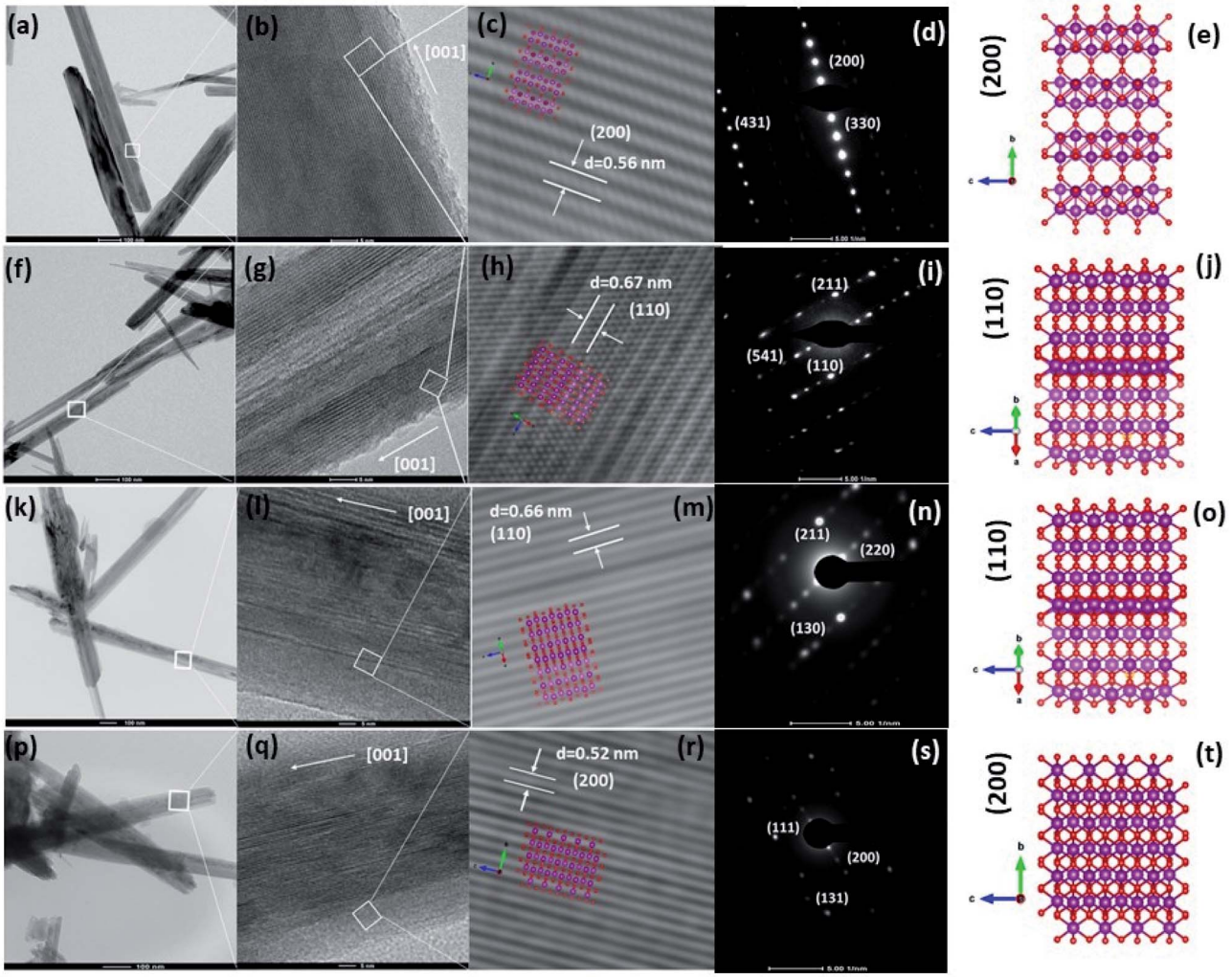

Fig. 13 Structural analysis of $Mn_{1-x}Fe_xO_2$: (a, f, k and p) TEM, (b, g, l and q) HRTEM, (c, h, m and r) lattice fringes related to the plane, (d, i, n and s) SAED patterns, and (e, j, o and t) illustrations of the crystal planes.

a parallel combination of resistance (R_g) and the capacitance (C_g) of grains, and the second consists of a parallel combination of resistance (R_{gb}) and the capacitance (C_{gb}) of the grain boundary. Finally, the electrode equivalence circuit parallel to R_e and C_e arises at a low frequency. In this circuit model, the wiring system provides equal responsibility for all samples. When the material is conductive, the wiring response is excellent, disappearing when the material becomes resistive. From this figure, the DC grain conductivity (σ_g in S cm^{-1}) of the samples can be deduced, and these are 4×10^{-2}, 1.67×10^{-2}, 3.2×10^{-3}, and 4.5×10^{-5} for $x = 0$, 0.05, 0.10, and 0.15, respectively, as shown in Fig. 15a. It is well-known that the conductivity can be determined by elementary charges and defect mobility. The decrease in the conductivity is related to the number of defects ($V_O^{\bullet\bullet}$) in the Fe-doped sample, due to the low mobility. However, the sharp drop in σ_g for $x = 0.15$ is attributed to a further combination of the phase transformation from initial α-MnO_2 to R-MnO_2. Furthermore, in the low x samples, the conductivity displayed higher values, since the large tunnel (2×2) facilitates the movement of K^+ ions in the α-MnO_2 structure.

In the XRD analysis, it has been explained that the addition of Fe-doping causes an increase in lattice strains, dislocations, and oxygen vacancies. This defect causes the diffusion process to be obstructed, and thus explains the conductivity reductions ($x = 0.05$–0.10). Furthermore, considering the XPS and XANES analyses described earlier, the mixed oxidation states of Fe and Mn were 3+/4+. The AC conductivity was related to the hopping of electrons between Fe^{4+} and Fe^{3+}, and the hopping rate increases with an increase of applied frequency. The substitution of Fe^{3+} at the Mn-site reduces the Mn^{4+} concentration due to electron exchange. In addition, the electron hopping energy between Fe^{3+} is larger than that between Mn^{4+}.[49] By increasing the replacement of Mn by Fe ions in the octahedral structure, the number of Mn ions is decreased, thereby defeating the electron exchange. Hence, the electrical conductivity is seen to decrease with an increase in Fe content.

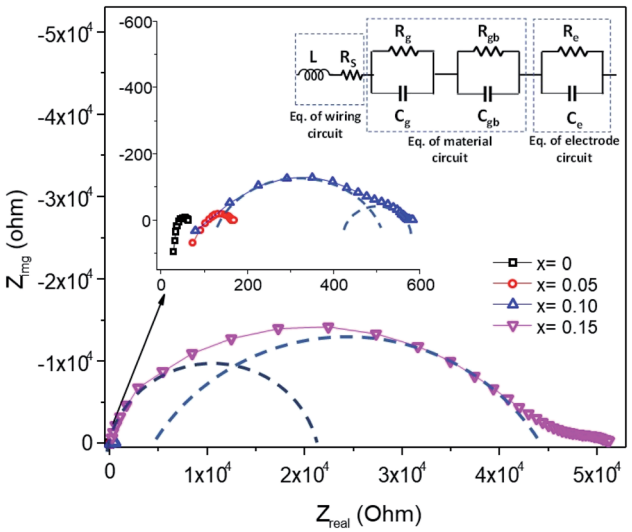

Fig. 14 Impedance spectra of $Mn_{1-x}Fe_xO_2$, and the equivalence electrical circuit model is indicated. The dashed line guides a single RC loop response.

The AC conductivity (σ_{AC}) can be calculated from the real and the imaginary parts of the impedance data, using the equation:[50]

$$\sigma_{AC} = \frac{t}{S}\left(\frac{Z'}{Z'^2 + Z''^2}\right) \quad (4)$$

where t = sample thickness, and S = surface cross-section. Fig. 15b shows the conductivity analysis for the MnO_2 nanorod and the Fe-doped sample, revealing the frequency dependent behavior. At a large domain of low frequency, the conductivity is low due to trapped charges in the defects (oxygen vacancies), while increasing the frequency increases the conductivity of the sample because the applied field provides enough energy to the trapped charge carriers in the defects, liberating them to enhance the conductivity. According to the hopping phenomenon, the hopping process between Mn^{3+}/Mn^{4+} ions increases with increasing frequency of the applied field.[51] Interestingly, at x = 0–0.05, the conductivity decreases at high frequencies. This is probably due to the number of ions diffusing more, causing the carrier mobility that is associated with transport to decrease.[52] Moreover, at $x = 0.15$, the phase transformation from α-MnO_2 to R-MnO_2 significantly affects the conductivity of the sample. A small tunnel (2×1) at R-MnO_2 inhibits the ion diffusion process.

In order to elucidate the applicable parameter capacitance C, since it is related proportionally to the permittivity through the basic relation, $C = \varepsilon A/d$, the following analysis was carried out on permittivity. The dielectric constant (ε_r) was measured as a function of the frequency at different Fe-doped concentrations, as shown in Fig. 16a, while the corresponding dielectric losses (tan δ) are depicted in Fig. 16c. It was observed that the dielectric constant of all the samples decreases with increasing frequency, and then it maintains an almost constant value in the high-frequency region. As is generally described through the Clausius–Mosotti equation, the permittivity of ceramic materials involves interfacial polarization p_i, dipole polarization p_d, atomic polarization p_a, and electronic polarization p_e. These polarizations affect the permittivity at low frequencies for p_i, up to the optical frequency range for p_a, respectively. The higher value of ε_r at a low frequency can be explained based on the interfacial/space charge polarization due to the inhomogeneous dielectric structure. The polarization decreases with an increase in frequency and reaches a constant value. This can be attributed to the fact that the material comprises multiple defects (Fe'_{Mn}, Mn'_{Mn}, Mn''_{Mn}, and $V_O^{\bullet\bullet}$) inducing inhomogeneous defect dipole creation beyond a certain external field frequency, and so the hopping dipoles cannot follow the frequency of the external electric field. At $x = 0$, the contribution of the space charge effect on polarization increases. The amount of doping causes the interfacial polarization to decrease gradually due to dipole polarization, p_d, created by the existing defect, as described

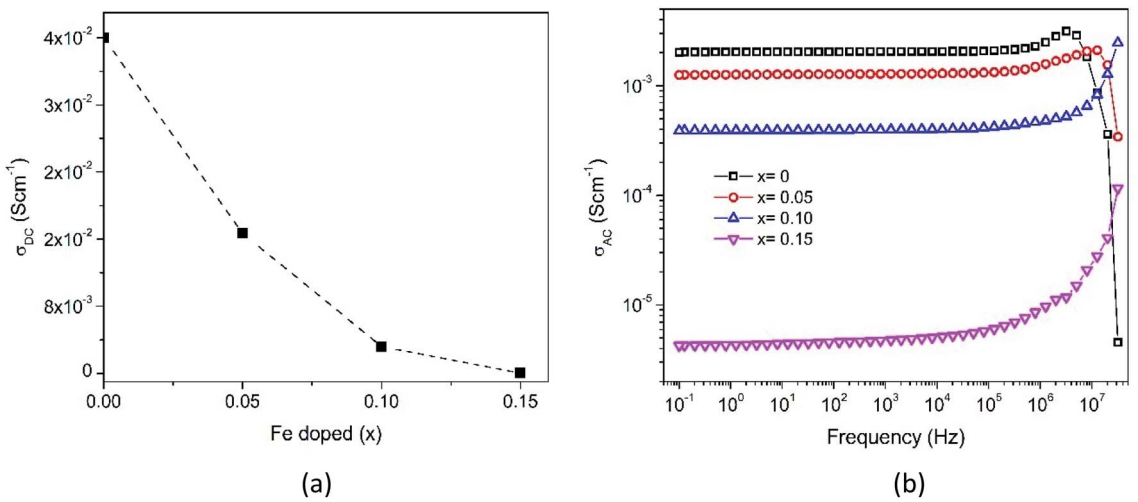

Fig. 15 Frequency-dependent (a) DC grain conductivity and (b) AC conductivity spectra of $Mn_{1-x}Fe_xO_2$.

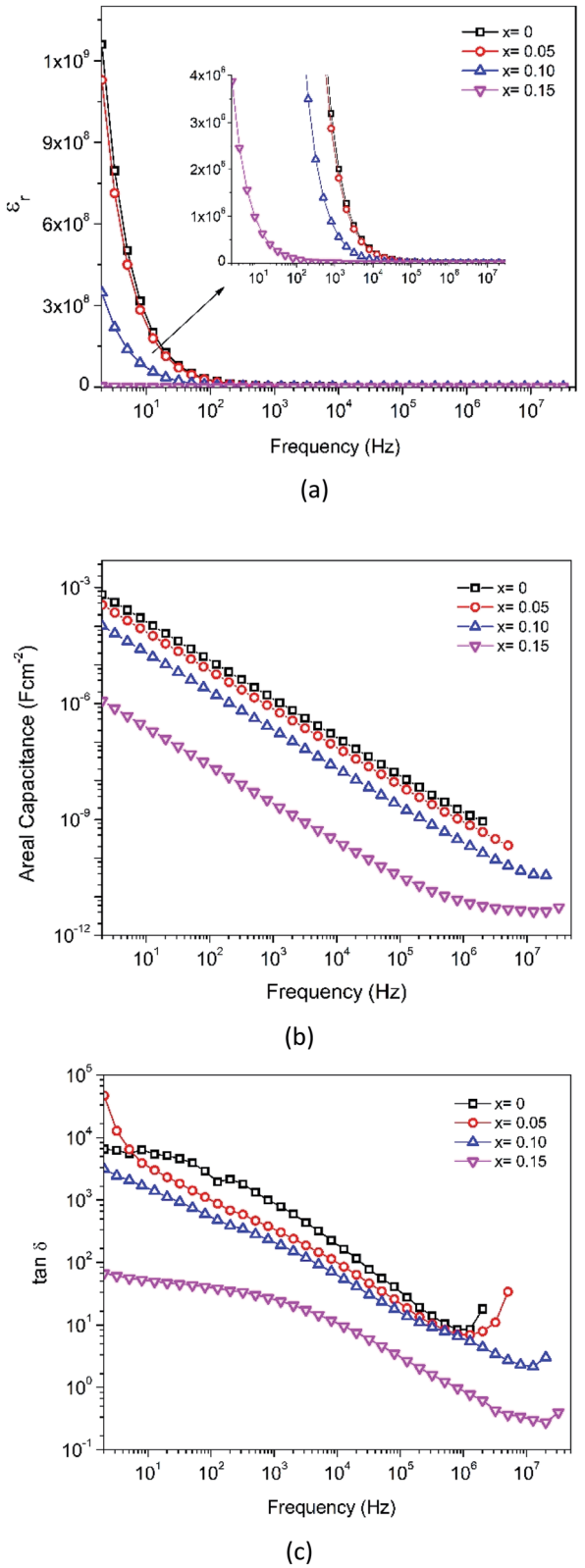

Fig. 16 (a) Dielectric constant, (b) dissipation factor and (c) areal capacitance as functions of frequency.

earlier in the doped samples. In addition, a significant disruption in the permittivity for $x = 0.15$ is associated with a combination of dipole defects and phase transformation to R-MnO_2 from the initial α-MnO_2. The areal capacitance as a function of frequency can be deduced from $C/A = \varepsilon_r\varepsilon_0/d$ and is presented in Fig. 16b.

The dielectric loss, or tan δ, represents the energy dissipation in the dielectric system. The loss tangent decreases continuously with increasing frequency, and the absence of Debye characteristics signifies a diffuse transition between the interfacial dipole and dipole polarization. The dispersion in tan δ is seen in the lower frequency region. A maximum value of tan δ can be observed only when the hopping frequency is equal to that of the externally applied electric field.

4. Conclusions

In summary, Fe-doped MnO_2 was successfully prepared using a hydrothermal method. Substituting longer radius Fe ions for Mn ions in the octahedral site causes increasing micro-strain, dislocation density, and oxygen vacancies that cause tunnel destruction, resulting in a phase transformation from the α-MnO_2 performing tunnel (2 × 2) to R-MnO_2 with a (2 × 1) tunnel. The oxidation state of the cations in the octahedron sites, Mn as well as Fe, possess a mixed oxidation state of 3+ and 4+. This creates the defects Fe'_{Mn} and $V_O^{\bullet\bullet}$, as well as the formation of Jahn–Teller distortion of Mn^{4+} to Mn^{3+}, which affects the electrical properties of Fe-doped MnO_2. MnO_2 without doping results in highly conductive samples. The addition of Fe-doping produces the formation of a defect and a reduced oxidation state, resulting in a material with lower conductivity and a lower dielectric constant.

Author contributions

E. Hastuti (conceptualization, data curation, formal analysis, investigation, methodology, resources, software, visualization, writing – original draft, writing – review & editing); A. Subhan (data curation, formal analysis, methodology, resources); P. Amonpattaratkit (data curation, formal analysis, methodology, resources); M. Zainuri (conceptualization, supervision, validation, writing – review & editing); S. Suasmoro (conceptualization, formal analysis, funding acquisition, methodology, project administration, resources, supervision, validation, visualization, writing – original draft, writing – review & editing).

Conflicts of interest

There are no conflicts to declare.

Acknowledgements

This research is supported by the Indonesian Ministry of Research and Higher Education through the Doctorate Dissertation program. The authors would like to thank the Research Center for Physics, Indonesian Institute for Science (LIPI) for microscopy analysis, and the SUT-NANOTEC-SLRI joint research facility for synchrotron utilization, Thailand, for XAS beam time.

References

1 X. Zheng, L. Yu, B. Lan, G. Cheng, T. Lin, B. He, W. Ye, M. Sun and F. Ye, *J. Power Sources*, 2017, **362**, 332–341.
2 S. Cheng, L. Yang, D. Chen, X. Ji, Z. Jiang, D. Ding and M. Liu, *Nano Energy*, 2014, **9**, 161–167.
3 A. González, E. Goikolea, J. A. Barrena and R. Mysyk, *Renewable Sustainable Energy Rev.*, 2016, **58**, 1189–1206.
4 M. Jayalakshmi and K. Balasubramanian, *Int. J. Electrochem. Sci.*, 2008, **3**, 22.
5 C. Julien and A. Mauger, *Nanomaterials*, 2017, **7**, 396.
6 S. J. A. Figueroa, F. G. Requejo, E. J. Lede, L. Lamaita, M. A. Peluso and J. E. Sambeth, *Catal. Today*, 2005, **107–108**, 849–855.
7 C. Sun, Y. Zhang, S. Song and D. Xue, *J. Appl. Crystallogr.*, 2013, **46**, 1128–1135.
8 G. Wang, G. Shao, J. Du, Y. Zhang and Z. Ma, *Mater. Chem. Phys.*, 2013, **138**, 108–113.
9 H. Yuan, L. Deng, Y. Qi, N. Kobayashi and M. Hasatani, *Int. J. Electrochem. Sci.*, 2015, **10**, 14.
10 A. I. Ivanets, T. F. Kuznetsova and V. G. Prozorovich, *Russ. J. Phys. Chem. A*, 2015, **89**, 481–486.
11 R. Poonguzhali, N. Shanmugam, R. Gobi, A. Senthilkumar, G. Viruthagiri and N. Kannadasan, *J. Power Sources*, 2015, **293**, 790–798.
12 T. M. Benedetti, V. R. Gonçales, D. F. S. Petri, S. I. C. de Torresi and R. M. Torresi, *J. Braz. Chem. Soc.*, 2010, **21**, 1704–1709.
13 S. B. Tarwate, S. S. Wahule, K. P. Gattu, A. V. Ghule and R. Sharma, *AIP Conf. Proc.*, 2018, **1953**, 030052.
14 S. Birgisson, D. Saha and B. B. Iversen, *Cryst. Growth Des.*, 2018, **18**, 827–838.
15 T. Kohler and T. Armbruster, *J. Solid State Chem.*, 1997, **133**, 486–500.
16 M. H. Alfaruqi, S. Islam, V. Mathew, J. Song, S. Kim, D. P. Tung, J. Jo, S. Kim, J. P. Baboo, Z. Xiu and J. Kim, *Appl. Surf. Sci.*, 2017, **404**, 435–442.
17 J. Yang, J. Wang, S. Ma, B. Ke, L. Yu, W. Zeng, Y. Li and J. Wang, *Phys. E*, 2019, **109**, 191–197.
18 T. Wang, H. C. Chen, F. Yu, X. S. Zhao and H. Wang, *Energy Storage Materials*, 2019, **16**, 545–573.
19 J. Dong, Z. Hou, Q. Zhao and Q. Yang, *E3S Web Conf.*, 2019, **79**, 03002.
20 A. M. A. Hashem, H. A. Mohamed, A. Bahloul, A. E. Eid and C. M. Julien, *Ionics*, 2008, **14**, 7–14.
21 J. U. Choi, C. S. Yoon, Q. Zhang, P. Kaghazchi, Y. H. Jung, K.-S. Lee, D.-C. Ahn, Y.-K. Sun and S.-T. Myung, *J. Mater. Chem. A*, 2019, **7**, 202–211.
22 P. Gao, P. Metz, T. Hey, Y. Gong, D. Liu, D. D. Edwards, J. Y. Howe, R. Huang and S. T. Misture, *Nat. Commun.*, 2017, **8**, 14559.
23 A. Khan, A. M. Toufiq, F. Tariq, Y. Khan, R. Hussain, N. Akhtar and S. ur Rahman, *Mater. Res. Express*, 2019, **6**, 065043.
24 Z. Li, A. Gu, Z. Lou, J. Sun, Q. Zhou and K. Y. Chan, *J. Mater. Sci.*, 2017, **52**, 4852–4865.
25 Z. Wang, F. Wang, Y. Li, J. Hu, Y. Lu and M. Xu, *Nanoscale*, 2016, **8**, 7309–7317.
26 F. Fitriana, M. Zainuri, M. A. Baqiya, M. Kato, P. Kidkhunthod and S. Suasmoro, *Bull. Mater. Sci.*, 2020, **43**, 152.
27 M. Klinger, *J. Appl. Crystallogr.*, 2017, **50**, 1226–1234.
28 S. Rong, P. Zhang, F. Liu and Y. Yang, *ACS Catal.*, 2018, **8**, 3435–3446.
29 L. Lutterotti, *Acta Crystallogr., Sect. A: Found. Crystallogr.*, 2000, **56**, s54.
30 D. Mondal, B. K. Paul, S. Das, D. Bhattacharya, D. Ghoshal, P. Nandy, K. Das and S. Das, *Langmuir*, 2018, **34**, 12702–12712.
31 K. Momma and F. Izumi, *J. Appl. Crystallogr.*, 2011, **44**, 1272–1276.
32 D. P. Dubal, W. B. Kim and C. D. Lokhande, *J. Phys. Chem. Solids*, 2012, **73**, 18–24.
33 N. Rajamanickam, P. Ganesan, S. Rajashabala and K. Ramachandran, 2014, 5.
34 T. Gao, M. Glerup, F. Krumeich, R. Nesper, H. Fjellvåg and P. Norby, *J. Phys. Chem. C*, 2008, **112**, 13134–13140.
35 A. M. Toufiq, F. Wang and H. U. Shah, *Phys. Status Solidi C*, 2017, 3.
36 J. E. Post, D. A. McKeown and P. J. Heaney, *Am. Mineral.*, 2020, **105**, 1175–1190.
37 C. Julien and M. Massot, *Phys. Chem. Chem. Phys.*, 2002, **4**, 4226–4235.
38 R. Selvamani, G. Singh, V. Sathe, V. S. Tiwari and P. K. Gupta, *J. Phys.: Condens. Matter*, 2011, **23**, 055901.
39 M. A. G. Soler and F. Qu, in *Raman Spectroscopy for Nanomaterials Characterization*, ed. C. S. S. R. Kumar, Springer, Berlin, Heidelberg, 2012, pp. 379–416.
40 N. Jain and A. Roy, *Phase & Morphology Engineered Surface Reducibility of MnO_2 Nano-heterostructures: Implications on Catalytic Activity Towards CO Oxidation*, 2019.
41 E. Beyreuther, S. Grafström, L. M. Eng, C. Thiele and K. Dörr, *Phys. Rev. B*, 2006, **73**, 155425.
42 N. Vilas Bôas, J. B. Souza Junior, L. C. Varanda, S. A. S. Machado and M. L. Calegaro, *Appl. Catal., B*, 2019, **258**, 118014.
43 R. A. Davoglio, G. Cabello, J. F. Marco and S. R. Biaggio, *Electrochim. Acta*, 2018, **261**, 428–435.
44 G. Yan, Y. Lian, Y. Gu, C. Yang, H. Sun, Q. Mu, Q. Li, W. Zhu, X. Zheng, M. Chen, J. Zhu, Z. Deng and Y. Peng, *ACS Catal.*, 2018, **8**, 10137–10147.
45 M. A. Farid, H. Zhang, X. Lin, A. Yang, S. Yang, F. Liao and J. Lin, 2012, 7.
46 R. Zhang, X. Yu, K.-W. Nam, C. Ling, T. S. Arthur, W. Song, A. M. Knapp, S. N. Ehrlich, X.-Q. Yang and M. Matsui, *Electrochem. Commun.*, 2012, **23**, 110–113.
47 H.-E. Nieminen, V. Miikkulainen, D. Settipani, L. Simonelli, P. Hönicke, C. Zech, Y. Kayser, B. Beckhoff, A.-P. Honkanen, M. J. Heikkilä, K. Mizohata, K. Meinander, O. M. E. Ylivaara, S. Huotari and M. Ritala, *J. Phys. Chem. C*, 2019, **123**, 15802–15814.

48 R. E. John, A. Chandran, J. George, A. Jose, G. Jose, J. Jose, N. V. Unnikrishnan, M. Thomas and K. C. George, *Phys. Chem. Chem. Phys.*, 2017, **19**, 28756–28771.
49 Y. Xie, Y. Jin and L. Xiang, *Crystals*, 2017, **7**, 221.
50 A. Rahal, S. M. Borchani, K. Guidara and M. Megdiche, *R. Soc. Open Sci.*, 2018, **5**, 171472.
51 S. I. Shah, S. Zulfiqar, T. Khan, R. Khan, S. A. Khan, S. A. Khattak and G. Khan, *J. Mater. Sci.: Mater. Electron.*, 2019, **30**, 19199–19205.
52 R. E. John, A. Chandran, M. Samuel, M. Thomas and K. C. George, *Phys. E*, 2020, **116**, 113720.